Statistical Design of Position-Encoded Microsphere Arrays at Low Target Concentrations

Xiaoxiao Xu, Pinaki Sarder, and Arye Nehorai*

***Abstract*—We design microsphere arrays with predetermined positions of microspheres, for capturing targets at low concentrations. To optimize the design parameters, we compute the Ziv-Zakai bound (ZZB) on the errors in estimating the target concentrations. We numerically demonstrate our design by computing the minimal distance between the microspheres and the optimal imaging temperature, for a desired level of errors. We also validate that, at low target concentrations, the statistical design using the ZZB is more precise than that using the posterior Cramér-Rao bound. We further quantitatively evaluate the effect of the fluorescence microscope point-spread function on the design performance, which provide useful guides to the device design and implementation. The key advantages of the proposed microsphere arrays are error-free target identification, simplified data analysis, high packing density, and reduced cost.**

I. Introduction

Microsphere arrays are used to detect and analyze concentrations of targets, such as mRNAs, proteins, antibodies and cells [1]. They have numerous applications including fundamental research, medical diagnostics, and drug discovery [2]. Compared with the conventional two-dimensional (2D) microarrays, microsphere arrays enable faster reaction due to their higher surface-to-volume ratio. However, in most existing microsphere arrays, the microspheres are placed randomly on a substrate [1]. The random placement makes their packing inefficient and subsequent data processing complicated. For example, imaging the randomly placed and clustered microspheres requires complex segmentation [3]. In addition, the microspheres are embedded with quantum-dot (QD) barcodes to identify the targets. The noise in their measured QD spectra makes them vulnerable to errors in identifying targets [4].

To overcome these drawbacks, we designed microsphere arrays with predetermined positions of the microspheres. We termed this feature position-encoding [5]. The distance between the position-encoded microspheres can be optimized to increase packing efficiency. These microspheres then capture specific targets of interest, and their predetermined positions help identify targets without errors. The error-free identification feature also simplifies the complex image segmentation and data analysis. Furthermore, the microsphere arrays enable simultaneous detection and quantification of multiple types of targets, by coding microspheres with different receptors; this is impossible for existing microsphere arrays [1].

In our previous work, we designed the position-encoded microsphere arrays by computing the posterior Cramér-Rao bound (PCRB) [6] on the mean-square error (MSE) in estimating the concentrations of captured targets. At high signal-to-noise ratio (SNR), the PCRB can be achieved asymptotically by the maximum likelihood estimates (MLE) of the concentrations. However, the PCRB only analyzes the local MSE, and it is not accurate at low SNR, particulary when the target concentration is low [7]. Thus, our previous design is applicable to limited scenarios. Nevertheless, in reasonable biological experiments, the concentrations of biological targets in the microarray are typically low [8], yielding low SNR signals in the captured images. Therefore, the PCRB cannot precisely characterize the statistical performance of our device, hindering us from accurately choosing design parameters.

To mitigate this limitation, we propose using the Ziv-Zakai bound (ZZB) [9] as the performance measure in our design. The ZZB is useful in analyzing the global MSE performance of a minimum MSE estimator for a statistical model. It is tight under all SNRs and it provides the asymptotic SNR threshold below which the MSE increases sharply [7]. Therefore, we anticipate that the ZZB is superior to the PCRB in precisely bounding the MSE of the target concentration estimation. Consequently, the ZZB allows us to accurately choose design parameters, such as the minimal distance between the microspheres and the optimal imaging temperature under a desired error, which ensures high packing density and minimizes device cost. Based on the ZZB, we further study the influences of the microscope point-spread function (PSF) [10] and image sensor resolution on the device performance, which provide valuable guides to device implementation practice.

In Section II, we introduce the configuration of the microsphere arrays. In Section III, we derive the ZZB model for the performance analysis. In Section IV, we use a numerical example to compare the design using the ZZB to that using the PCRB. We also discuss the strategies to choose the design parameters. Finally, we conclude in Section V.

II. Microsphere Arrays Configuration

In this section, we review the configuration of microsphere arrays and their image acquisition process. Fig. 1(a) shows the uniform 2D grid layout for the microspheres arrays. The microspheres ($\sim$5 μm in diameter) are made of polystyrene. They are placed in predetermined positions and are encoded by dedicated receptors to capture targets of interest (Fig. 1(b)).

Asterisk indicates corresponding author.

Xiaoxiao Xu (xiaoxu@ese.wustl.edu) and Arye Nehorai (nehorai@ese.wustl.edu) are with the Department of Electrical and Systems Engineering, Washington University in St. Louis, St. Louis, MO 63130.

Pinaki Sarder (sarderp@mir.wustl.edu) is with the Mallinckrodt Institute of Radiology, Washington University School of Medicine in St. Louis, MO 63110.

This work was supported by the National Science Foundation Grant CCF0963742.

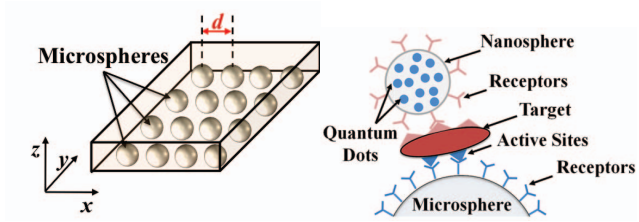

(a) (b)

Fig. 1: Schematic diagram of the proposed position-encoded microsphere arrays. (a) 2D Layout. (b) A target molecule captured on a microsphere.

The receptors are antibody molecules. To detect and quantify the targets, nanospheres (~100 nm in diameter) are embedded with identical QDs and conjugated with receptors. These QD-embedded nanospheres allow label-free targeting and enhance the detection sensitivity.

To perform the detection, we pass a microfluid stream with the targets through the microsphere arrays and periodically release a cocktail of nanospheres. In this flow process, the targets are captured by the intended microspheres on one side and tagged by the nanospheres on the other. Then, all nanospheres' QDs emit light upon excitation by UV light, and the emitted light is in the form of a spherical shell around each microsphere.

To image the target-captured specimen, we focus a fluorescence microscope at different depth planes of the arrays, parallel to the xy plane of the device in Fig. 1(a). We then collect a series of 2D cross-section images of the lights emitted by the nanospheres' QDs. Thus, each cross-section image of the shell light around a microsphere forms an image of a ring. The levels of the light intensities are proportional to the target concentrations on the microspheres.

We employ a CMOS image sensor [11] to capture the images. In the image acquisition, the researchers in [1] employed expensive, cooled CCD detectors. Alternatively, we use inexpensive CMOS image sensors. These sensors have high sensitivity, but produce greater noise and require cooling using external electronics. To minimize the cost, we use the performance measure to select the optimal temperature T_{opt} as a trade-off between minimal cooling vs. maximal accuracy.

III. Performance Analysis

In this section, we first present the statistical measurement model in estimating the target concentrations from the microsphere arrays. Then we derive the ZZB performance measure on the corresponding MSE.

A. Measurement Model

The measurement at the image sensor output, in fluorescence microscopy imaging of the illuminating object [3] is

$$g(x,y,z;\boldsymbol{\theta}) = \tilde{s}(x,y,z;\boldsymbol{\theta}) + w_{\text{b}}(x,y,z;\boldsymbol{\theta}), \tag{1}$$

where, $x \in \{x_1, x_2, \ldots, x_K\}$, $y \in \{y_1, y_2, \ldots, y_L\}$, and $z \in \{z_1, z_2, \ldots, z_M\}$; K, L and M denote the numbers of measurement voxels, and $\tilde{s}(x,y,z;\boldsymbol{\theta})$ is the microscope output

$$\tilde{s}(x,y,z;\boldsymbol{\theta}) = s(x,y,z;\boldsymbol{\theta}) \otimes h(x,y,z), \tag{2}$$

where $s(x,y,z;\boldsymbol{\theta})$ is the illuminating object, $h(x,y,z)$ is the fluorescence microscope PSF, $\otimes$ is the convolution operation, and $w_{\text{b}}(x,y,z;\boldsymbol{\theta})$ is the background noise.

1) *Object Model*: Recall that the target concentrations on the microspheres are proportional to the intensity levels of the shell lights. Therefore, the object model for two neighboring microspheres is given by

$$s(x,y,z;\boldsymbol{\theta}) = s_{\text{sh}}(x,y,z;\theta_1) + s_{\text{sh}}(x-d,y,z;\theta_2), \tag{3}$$

where, d is the distance between the two microspheres. $\boldsymbol{\theta} = [\theta_1, \theta_2]^T$, θ_1 and θ_2 are the unknown intensity levels per voxel of the single shells $s_{\text{sh}}(x,y,z;\theta_1)$ and $s_{\text{sh}}(x-d,y,z;\theta_2)$, respectively. The single shell is

$$s_{\text{sh}}(x,y,z;\theta_i) = \begin{cases} \theta_i & \text{if } r_1 < \sqrt{x^2+y^2+z^2} < r_2 \\ 0 & \text{otherwise} \end{cases} \tag{4}$$

where $i \in 1, 2$ indexes the two neighboring microspheres.

In general, no additional information other than the maximum intensity levels θ_{max} are available, so we adopt a uniform prior distribution for θ_i of the ith shell; $\theta_i \sim \mathcal{U}(0, \theta_{\text{max}})$, $\forall i \in 1, 2$. Thus, we express the object model as

$$\begin{aligned} s(x,y,z;\boldsymbol{\theta}) &= \boldsymbol{o}(x,y,z,d) \cdot \boldsymbol{\theta} \\ \boldsymbol{o}(x,y,z,d) &= [I_{[r_1 < \sqrt{x^2+y^2+z^2} < r_2]}(x,y,z,d), \\ &\quad\; I_{[r_1 < \sqrt{(x-d)^2+y^2+z^2} < r_2]}(x,y,z,d)], \end{aligned} \tag{5}$$

where $I_A(\cdot)$ is an indicator function.

The microscope output is given by

$$\tilde{s}(x,y,z;\boldsymbol{\theta}) = \boldsymbol{s}'(x,y,z,d) \cdot \boldsymbol{\theta}, \tag{6}$$

where $\boldsymbol{s}'(\cdot) = \boldsymbol{o}(x,y,z,d) \otimes h(x,y,z)$.

2) *PSF Model*: We consider the PSF to be 3D Gaussian [10]

$$h(x,y,z;\sigma_1^2,\sigma_2^2) = \exp\left(-\frac{x^2+y^2}{2\sigma_1^2} - \frac{z^2}{2\sigma_2^2}\right), \tag{7}$$

where σ_1^2 and σ_2^2 are known parameters of the PSF function. This model preserves the symmetry and the asymmetry of the classical Gibbson and Lanni PSF model along the focal planes and the optical direction, respectively.

3) *Noise Model*: Assuming ideal operation in the imaging process, the external noise sources (the scattered excitation and background light) are eliminated. Additionally, we ignore the intrinsic noises such as the flicker $(1/f)$ and dark current, as they can be largely eliminated in current sensors [11]. Furthermore, we focus on low light intensity so that the shot noise is negligible [12]. Therefore, in our design, the dominant source of noise is reset and readout transistors thermal noise.

The thermal noise is modeled by $w_{\text{b}}(\cdot)$, which is zero-mean Gaussian with variance σ_{b}^2, and is independently and identically distributed from voxel to voxel. The noise level σ_{b}^2 is a function of temperature T [11]

$$\sigma_b^2(T) = kT/B, \tag{8}$$

where B is a constant that relates to the microscope and image sensor specifications and the external environment, and k is the Boltzmann constant. We assume B is known, or it

can be estimated from the images of target-free microspheres embedded with QDs.

Therefore, the measurement $g(x, y, z; \boldsymbol{\theta})$ is Gaussian distributed with mean $\boldsymbol{s}'(x, y, z, d) \cdot \boldsymbol{\theta}$ and variance σ_{b}^2, with SNR

$$\mathrm{SNR}_{\mathrm{dB}} = 10\log_{10}\left(\sum_{\substack{x,y,z:\boldsymbol{s}_i'(\cdot)>\delta \\ i=1,2}} \frac{(\boldsymbol{s}'(x, y, z, d) \cdot \boldsymbol{\theta}_{\max})^2}{4\sigma_{\mathrm{b}}^2 N}\right), \quad (9)$$

where δ is a small user-chosen constant and N is the number of voxels with $\boldsymbol{s}_i'(\cdot) > \delta$.

We group the measurements into a vector form

$$\boldsymbol{g} = \mathrm{S}'\boldsymbol{\theta} + \boldsymbol{w}_{\mathrm{b}}, \quad (10)$$

where $\boldsymbol{g}$ and $\boldsymbol{w}_{\mathrm{b}}$ are $(KLM \times 1)$-dimensional vectors whose $(KL((z-z_1)/\Delta z)+K((y-y_1)/\Delta y)+((x-x_1)/\Delta x)+1)^{\mathrm{th}}$ components are $g(\cdot)$ and $w_{\mathrm{b}}(\cdot)$, respectively; S' is a $(KLM \times 2)$ matrix whose $(KL((z-z_1)/\Delta z) + K((y-y_1)/\Delta y) + ((x-x_1)/\Delta x)+1)^{\mathrm{th}}$ row is $[\tilde{s_1'}(\cdot)\ \tilde{s_2'}(\cdot)]$. In these expressions, $\Delta x = (x_{k+1} - x_k)$ with $k \in \{1, 2, \ldots, K-1\}$; Δy and Δz are similar to Δx. Therefore, $\boldsymbol{g} \sim \mathcal{N}(\mathrm{S}'\boldsymbol{\theta}, \sigma_{\mathrm{b}}^2\mathbf{I})$, where $\mathbf{I}$ is the identity matrix.

B. The Ziv-Zakai Bound

We compute the ZZB on the MSE in estimating the unknown parameters $\boldsymbol{\theta}$ as the performance measure in our design. Below, we briefly present the concept of the ZZB [9]. Let $\boldsymbol{g}$ denote the measurement vector, and $\hat{\boldsymbol{\theta}}(\boldsymbol{g})$ denote the estimator of the unknown n-dimensional random vector $\boldsymbol{\theta} = [\theta_1, \theta_2, \ldots, \theta_n]^T$. Consider the estimation error $\boldsymbol{\epsilon} = \hat{\boldsymbol{\theta}}(\boldsymbol{g}) - \boldsymbol{\theta}$ with covariance matrix (MSE) $\mathbf{R}_{\boldsymbol{\epsilon}} = \mathrm{E}[\boldsymbol{\epsilon}\boldsymbol{\epsilon}^T]$, where the expectation $\mathrm{E}(\cdot)$ is over $\boldsymbol{g}$ and $\boldsymbol{\theta}$, and $\boldsymbol{\theta}$ has a known prior probability density function (pdf) $p_{\Theta}(\boldsymbol{\theta})$. Then, the ZZB is computed through the following inequality:

$$\begin{aligned}\boldsymbol{u}^T\mathbf{R}_{\boldsymbol{\epsilon}}\boldsymbol{u} \quad \geq \quad & \frac{1}{2}\int_0^{\infty} \mathcal{V}\Bigg\{\max_{\boldsymbol{e}:\boldsymbol{u}^T\boldsymbol{e}=b}\Bigg[\int_{\mathbb{R}^n}(p_{\boldsymbol{\theta}}(\boldsymbol{\eta}) \quad (11)\\ & +p_{\boldsymbol{\theta}}(\boldsymbol{\eta}+\boldsymbol{e}))P_{\min}(\boldsymbol{\eta}, \boldsymbol{\eta}+\boldsymbol{e})\mathrm{d}\boldsymbol{\eta}\Bigg]\Bigg\}b\mathrm{d}b,\end{aligned}$$

where $\boldsymbol{u}$ is any n-dimensional vector, $\mathcal{V}$ is a 'valley-filling' function, $\boldsymbol{e}$ is the offset, and $P_{\min}(\boldsymbol{\eta}, \boldsymbol{\eta}+\boldsymbol{e})$ is the minimum probability of error for the hypothesis test of a detection problem

$$\begin{aligned}\mathcal{H}_0 : \boldsymbol{\theta} = \boldsymbol{\eta} \qquad & \text{with } \boldsymbol{g} \sim p_{\boldsymbol{g}|\boldsymbol{\theta}}(\boldsymbol{g}|\boldsymbol{\eta}) \quad (12)\\ \mathcal{H}_1 : \boldsymbol{\theta} = \boldsymbol{\eta}+\boldsymbol{e} \qquad & \text{with } \boldsymbol{g} \sim p_{\boldsymbol{g}|\boldsymbol{\theta}}(\boldsymbol{g}|\boldsymbol{\eta}+\boldsymbol{e}),\end{aligned}$$

with $\Pr(\mathcal{H}_0) = p_{\boldsymbol{\theta}}(\boldsymbol{\eta})/(p_{\boldsymbol{\theta}}(\boldsymbol{\eta}) + p_{\boldsymbol{\theta}}(\boldsymbol{\eta}+\boldsymbol{e})) = 1 - \Pr(\mathcal{H}_1)$.

It is generally challenging to derive a closed-form expression of the general bound (11), because analytically deriving $P_{\min}(\cdot)$ and computing $\mathcal{V}(\cdot)$ and the related integral are difficult. In many practical cases, however, a weaker bound is derived by omitting $\mathcal{V}(\cdot)$ and equating the prior probabilities of the hypothesis $\Pr(\mathcal{H}_0) = \Pr(\mathcal{H}_1) = \frac{1}{2}$. Consequently, $\frac{1}{2}(p_{\boldsymbol{\theta}}(\boldsymbol{\eta})+p_{\boldsymbol{\theta}}(\boldsymbol{\eta}+\boldsymbol{e}))$ is replaced with $\min(p_{\boldsymbol{\theta}}(\boldsymbol{\eta}), p_{\boldsymbol{\theta}}(\boldsymbol{\eta}+\boldsymbol{e}))$.

C. Performance Analysis using the Ziv-Zakai Bound

We employ the weaker ZZB and define the performance measure as the sum of the ZZBs on the MSEs in estimating θ_1 and θ_2. In other words, we use $\boldsymbol{u} = [1, 0]^T$ and $\boldsymbol{u} = [0, 1]^T$ to derive $\mathrm{ZZB}(\theta_1)$ and $\mathrm{ZZB}(\theta_2)$, respectively. Thus the performance measure is $P_{\mathrm{ZZB}} = \mathrm{ZZB}(\theta_1) + \mathrm{ZZB}(\theta_2)$. The offset is $\boldsymbol{e} = [e_1, e_2]^T$ with $e_1, e_2 \in [-\theta_{\max}\ \theta_{\max}]$. $P_{\min}(\boldsymbol{\eta}, \boldsymbol{\eta}+\boldsymbol{e})$ is obtained from the log likelihood-ratio test [6]

$$\begin{aligned}P_{\min} \quad &= \quad \frac{1}{2}\{\Pr(\Lambda > 0|\mathcal{H}_0) + \Pr(\Lambda < 0|\mathcal{H}_1)\} \quad (13)\\ &= \quad \mathrm{Q}\left(\frac{\sqrt{\boldsymbol{e}^T\mathrm{S}'^T\mathrm{S}'\boldsymbol{e}}}{2\sigma_{\mathrm{b}}}\right),\end{aligned}$$

where $\Lambda(\boldsymbol{g}, \boldsymbol{\theta}) = \log\frac{p(\boldsymbol{g}|\mathcal{H}_1)}{p(\boldsymbol{g}|\mathcal{H}_0)}$ and $\mathrm{Q}(z) = \int_z^{\infty}\frac{1}{\sqrt{2\pi}}e^{-\frac{s^2}{2}}\mathrm{d}s$. Note that $P_{\min}$ is only a function of the offset $\boldsymbol{e}$ between the hypotheses, so the equal hypothesis ZZB simplifies to

$$\boldsymbol{u}^T\mathbf{R}_{\boldsymbol{\epsilon}}\boldsymbol{u} \geq \int_0^{\theta_{\max}} \max_{\boldsymbol{e}:\boldsymbol{u}^T\boldsymbol{e}=b} \mathrm{A}(\boldsymbol{e})P_{\min}(\boldsymbol{e})b\mathrm{d}b, \quad (14)$$

where $\mathrm{A}(\boldsymbol{e}) = \int_{\mathbb{R}^2}\min(p_{\boldsymbol{\theta}}(\boldsymbol{\eta}), p_{\boldsymbol{\theta}}(\boldsymbol{\eta}+\boldsymbol{e}))\mathrm{d}\boldsymbol{\eta}$.

Recall that the prior distributions for θ_1 and θ_2 are uniform and independent, i.e., $p_{\Theta_1}(\theta_1) = p_{\Theta_2}(\theta_2) = \frac{1}{\theta_{\max}}$. Therefore, $\mathrm{A}(\boldsymbol{e})$ is expressed as

$$\mathrm{A}(\boldsymbol{e}) = \frac{(\theta_{\max} - |e_1|)(\theta_{\max} - |e_2|)}{\theta_{\max}^2}. \quad (15)$$

We use the grid-search method to find the $\max(\cdot)$ and numerically integrate the integral at a finite number of discrete points using Reimann sums.

Note that in our design, the prior distribution is uniform, and the valley-filling function $\mathcal{V}(\cdot)$ is trivial in (11) because the term inside it is nonincreasing in b. Therefore, the equal hypothesis bound in (14) is as tight as the general bound (11).

IV. Numerical Example

This simple example illustrates our concept for the statistical design and strategies to obtain the optimal design parameters. In particular, we propose a spherical object model for the shells, i.e., we let $r_1 = 0\ \mu\mathrm{m}$ and $r_2 = 2.5\ \mu\mathrm{m}$. We also use realistic values for design parameters from a training experiment [5] (the prior intensities, the background noise variance, the microscope PSF variance and the image sensor sampling voxels). Namely, we use $\theta_{\max} = 0.053$, $\sigma_{\mathrm{b}}^2 = 4.23 \times 10^{-4}$ at $T = 10\ ^{\circ}\mathrm{C}$, $\sigma_1^2 = 6\ \mu\mathrm{m}^2$, $\sigma_2^2 = 20\ \mu\mathrm{m}^2$, $\Delta x = \Delta y = 0.4\ \mu\mathrm{m}/\mathrm{pixel}$ and $\Delta z = 0.5\ \mu\mathrm{m}$. Therefore, the light intensity is low compared to the level of background noise; in other words, the SNR computed by (9) is low.

A. Comparison between Performance Measures Computed by ZZB and PCRB

To illustrate that the design using the ZZB outperforms that using the PCRB at low target concentrations (low SNRs), we compare the corresponding performance measures P_{ZZB} and P_{PCRB}. We have derived P_{ZZB} in section III, and P_{PCRB} is [5]

$$P_{\mathrm{PCRB}} = \mathrm{trace}(J^{-1}), \quad (16)$$

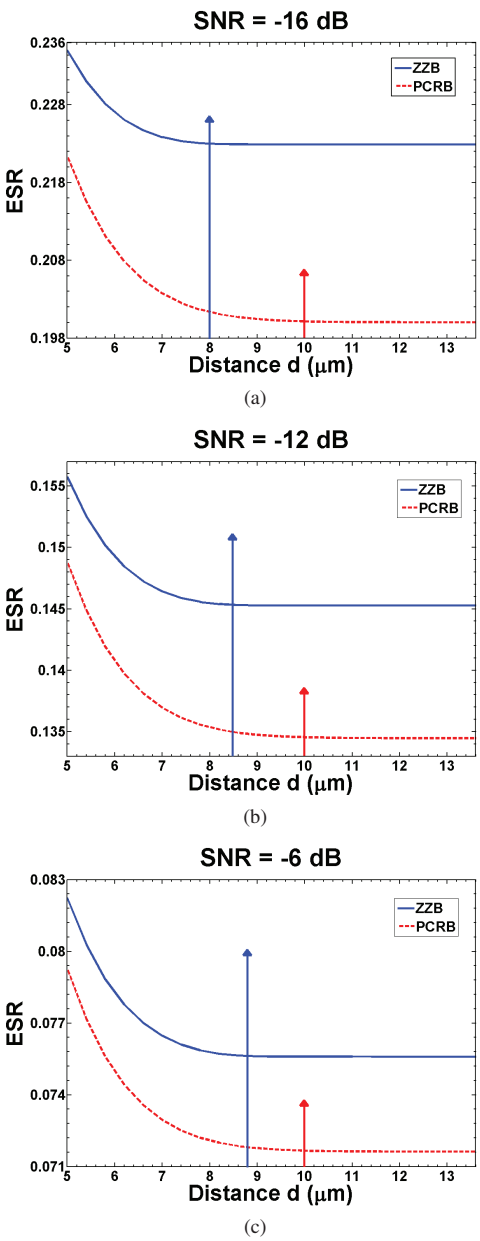

Fig. 2: Comparisons between Ziv-Zakai Bound and Posterior Cramér-Rao Bound as a function of distance d under increasing SNRs from (a)-(c). Arrows indicate d_{opt}.

where J is the Fisher information matrix with elements

$$J_{ij} = \mathrm{E}_{\boldsymbol{\theta}}\left[\sum_z \sum_y \sum_x \left(\frac{\boldsymbol{s}_i' \boldsymbol{s}_j'}{\sigma_{\mathrm{b}}^2}\right)\right], \qquad i,j = 1,2. \tag{17}$$

$\mathrm{E}_{\boldsymbol{\theta}}[\cdot]$ is the expectation with respect to the pdf $p_{\Theta}(\boldsymbol{\theta})$. We define the estimation error-to-signal ratio (ESR) as

$$ESR = \frac{\sqrt{\text{MSE bound}}}{0.5\theta_{\max}}. \tag{18}$$

Fig. 2(a)-(c) present P_{ZZB} and P_{PCRB} as a function of increasing SNRs. Generally, we observe that with the increase of d, $P_{\text{ZZB}}(d)$ and $P_{\text{PCRB}}(d)$ first decrease and then essentially flatten. Increased distance between the microspheres reduces the interactions between the shell lights. Therefore, the corresponding errors in estimating the light intensities decrease. As the interactions reduce to a negligible level compared to that of the background noise, which is invariant with respect to d, the errors flatten. Thus, we denote the flattening point as d_{opt}.

However, $P_{\text{ZZB}}(d)$ is always tighter than $P_{\text{PCRB}}(d)$ under different SNRs, especially at low SNRs. Moreover, as SNR increases, d_{opt} from $P_{\text{ZZB}}(d)$ increases, while there is a very slight change in d_{opt} from P_{PCRB} (around 10 μm). It should be noted that the shape and magnitude of $P_{\text{ZZB}}(d)$ eventually approach those of $P_{\text{PCRB}}(d)$ as SNR becomes large. Therefore, compared to P_{PCRB}, $P_{\text{ZZB}}(d)$ accurately resembles the MSE under all SNRs, which suggests that ZZB is a more applicable performance bound for our statistical design.

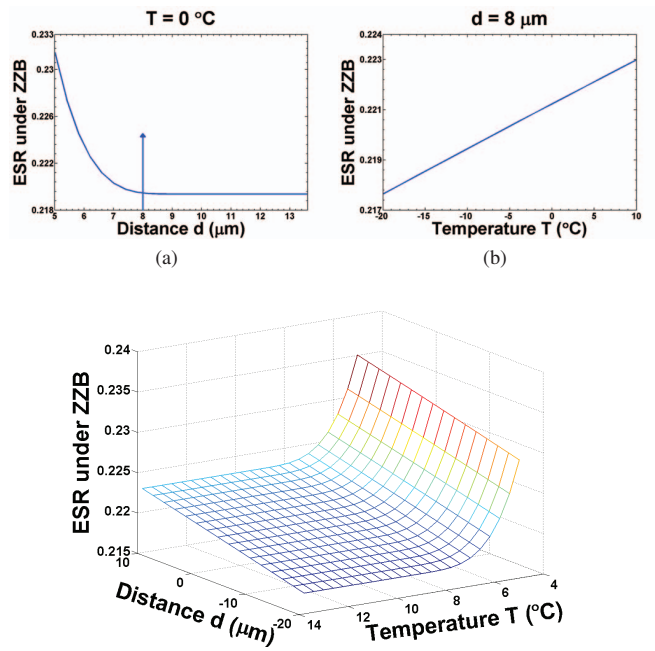

Fig. 3: Design Results. (a) Performance as a function of distance d at temperature $T = 0$ °C. The arrow indicates d_{opt}. (b) Performance as a function of T at $d = 8$ μm. (c) Performance as a function of T and d.

B. Selection of Optimal Distance and Imaging Temperature

Fig. 3(a) shows that the optimal distance d_{opt} between the microspheres is 8 μm, at the imaging temperature $T = 0$ °C. Fig. 3(b) presents the effect of T on the performance measure $P_{\text{ZZB}}(T)$, at a fixed distance $d = 8$ μm. We observe that the performance degrades with increased temperature. Therefore, temperature is a critical parameter for employing less expensive CMOS image sensors, while attaining a desired estimation accuracy.

Fig. 3(c) presents a 3D plot of the effects of the microspheres' distance and the imaging temperature on the statistical design performance.

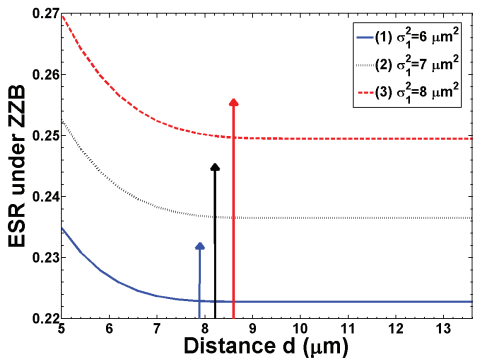

(a)

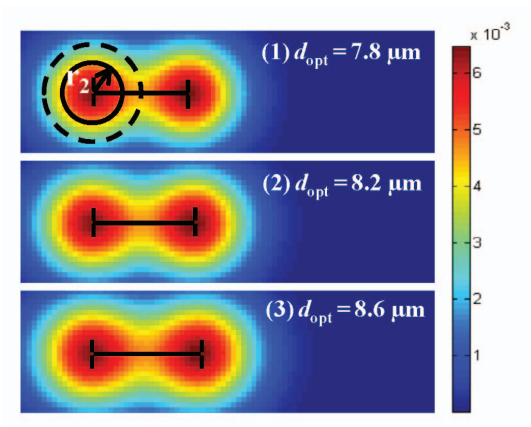

(b)

Fig. 4: Design Results. (a) Performance measure under different microscope PSF variance (1)-(3) as a function of distance d. Arrows indicate d_{opt}. (b) Simulated xy plane fluorescence intensity images of neighboring microspheres corresponding to (a)(1)-(3). The microspheres are separated at d_{opt}, at $z = 0\ \mu\text{m}$.

C. Influence of Microscope Point-Spread Function

In the fluorescence microscopy images, PSF often causes the most severe distortion. Due to the PSF, even an arbitrarily high magnification fluorescence microscopy cannot enable us to see infinitely small details [13]. Therefore, it is of great importance to understand the influence of the PSF in our design.

In Fig. 4(a), we present the performance measure under the microscope PSF variance $\sigma_1^2 = 6\ \mu\text{m}^2, 7\ \mu\text{m}^2, 8\ \mu\text{m}^2$ at different distances d, while keeping $\sigma_2^2 = 20\ \mu\text{m}^2$ fixed along the z-axis. The performance measure and optimal distance d_{opt} increase within σ_1^2, because larger PSF variance induces more blur around the illuminating objects, and thus the distance between microspheres has to be larger to reduce the interactions to a negligible level. Moreover, the performance seems more sensitive to the PSF variance than to the distance. Though a microscope of small PSF variance ensures good performance, it should be noted that this microscope may be sophisticated and costly [13]. Therefore, we need to choose the microscope PSF as a trade-off between cost and accuracy.

Fig. 4(b) presents the corresponding xy focal plane intensity images of the neighboring microspheres separated at d_{opt} and at $z = 0\ \mu\text{m}$, and it offers visualized illustration of how the PSF affects the imaging of the objects. Note that d_{opt} is smaller than the microsphere diameter after the PSF blur. For example, in Fig. 4(b)-(1), $d_{\text{opt}} = 7.8\ \mu\text{m}$. This smaller d_{opt} is expected, as we discussed in IV-A that d_{opt} is chosen at the flattening point, before the point at which the interactions completely disappear.

V. Conclusions

We presented the statistical design of position-encoded microsphere arrays for capturing targets at low concentrations. To optimize the design parameters, we computed the ZZB on the errors in estimating the target concentrations. With a numerical example, we verified that at low target concentrations the design using the ZZB is superior to that using the PCRB. In this example, we also demonstrated the strategies for choosing the minimal distance between the microspheres and the optimal imaging temperature, with a desired level of errors. We further quantitatively simulated that the microscope PSF has significant influences on the design performance. In our future work, we will conduct imaging experiments to validate the measurement model and compare the imaging performance of our device to that of existing ones.

References

[1] A. Mathur, *Image Analysis of Ultra-High Density, Multiplexed, Microsphere-Based Assays*, Ph.D. thesis, Northwestern Univ., Chicago, Sept. 2006.

[2] P. O. Brown and D. Botstein, "Exploring the new world of the genome with dna microarrays," *Nat. Genet.*, vol. 21, pp. 33–27, Jan. 1999.

[3] P. Sarder and A. Nehorai, "Estimating locations of quantum-dotcencoded microparticles from ultra-high density 3d microarrays," *IEEE Trans. Nanobiosci.*, vol. 7, pp. 284–297, Jan. 2008.

[4] K. D. Bake and D. R. Walt, "Multiplexed spectroscopic detections," *Annu. Rev. Anal. Chem.*, vol. 1, pp. 15–47, July 2008.

[5] P. Sarder and A. Nehorai, "Statistical design of position-encoded microsphere arrays," *IEEE Trans. Nanobiosci.*, vol. 10, pp. 16–29, Mar. 2011.

[6] H. L. van Trees, *Detection, Estimation and Modulation Theory*, John Wiley, New York, 1968.

[7] S. C. White and N. C. Beaulieu, "On the application of the cramer-rao and detection theory bounds to mean square error of symbol timing recovery," *IEEE Trans. Commun.*, vol. 40, pp. 1635–1643, Oct. 1992.

[8] J. A. Ferguson, F. J. Steemers, and D. R. Walt, "High-density fiber-optic dna random microsphere array," *Anal. Chem.*, vol. 72, pp. 5618–5624, Nov. 2000.

[9] K. L. Bell, Y. Steinberg, Y. Ephraim, and H. L. van Trees, "Extended zivzakai lower bound for vector parameter estimation," *IEEE Trans. Inf. Theory*, vol. 43, pp. 624–637, Mar. 1997.

[10] P. Sarder and A. Nehorai, "Deconvolution methods for 3-d fluorescence microscopy images," *IEEE Signal Process. Mag.*, vol. 23, pp. 32–45, May 2006.

[11] J. Ohta, *Smart CMOS Image Sensors and Applications*, CRC Press, Boca Raton, 2007.

[12] V. Gruev, Z. Yang, and J. Van. der Spiegel, "Current mode image sensor with two transistors per pixel," *IEEE Trans. Circuits Syst. I*, vol. 57, pp. 1154–1165, June 2010.

[13] B. Huang, M. Bates, and X. Zhuang, "Super-resolution fluorescence microscopy," *Annu. Rev. Biochem.*, vol. 78, pp. 993–1016, Apr. 2009.